Type Ia supernovae with and without blueshifted narrow Na I D lines – how different is their structure?

S. Hachinger[1,2,3], F. K. Röpke[1,4], P. A. Mazzali[5,6], A. Gal-Yam[7], K. Maguire[8,9],
M. Sullivan[10], S. Taubenberger[8,6], C. Ashall[5], H. Campbell[11], N. Elias-Rosa[12], U. Feindt[13],
L. Greggio[12], C. Inserra[9], M. Miluzio[12,14], S. J. Smartt[9], D. Young[9]

[1]*Institut für Theoretische Physik und Astrophysik, Universität Würzburg, Emil-Fischer-Str. 31, 97074 Würzburg, Germany*
[2]*Institut für Mathematik, Universität Würzburg, Emil-Fischer-Str. 30, 97074 Würzburg, Germany*
[3]*Leibniz Supercomputing Centre (LRZ), Bavarian Academy of Sciences and Humanities, Boltzmannstr. 1, 85748 Garching b. München, Germany*
[4]*Heidelberger Institut für Theoretische Studien, Schloss-Wolfsbrunnenweg 35, 69118 Heidelberg, Germany*
[5]*Astrophysics Research Institute, Liverpool John Moores University, IC2 Liverpool Science Park, 146 Brownlow Hill, Liverpool, L3 5RF, UK*
[6]*Max-Planck-Institut für Astrophysik, Karl-Schwarzschild-Str. 1, 85741 Garching, Germany*
[7]*Benoziyo Center for Astrophysics, Weizmann Institute of Science, 76100 Rehovot, Israel*
[8]*European Organisation for Astronomical Research in the Southern Hemisphere (ESO), Karl-Schwarzschild-Str. 2, 85748 Garching b. München, Germany*
[9]*School of Mathematics and Physics, Queen's University Belfast, Belfast BT7 1NN, UK*
[10]*Physics & Astronomy, University of Southampton, Southampton, Hampshire SO17 1BJ, UK*
[11]*Institute of Astronomy, University of Cambridge, Madingley Road, Cambridge CB3 0HA, UK*
[12]*INAF - Osservatorio Astronomico di Padova, vicolo dell'Osservatorio 5, 35122 Padova, Italy*
[13]*Oskar Klein Centre, Department of Physics, Stockholm University, Albanova University Center, 10691 Stockholm, Sweden*
[14]*Instituto de Astrofisica de Canarias, C/ Vía Láctea, s/n, 38205, La Laguna, Tenerife, Spain*

ABSTRACT

In studies on intermediate- and high-resolution spectra of Type Ia supernovae (SNe Ia), some objects exhibit narrow Na I D absorptions often blueshifted with respect to the rest wavelength within the host galaxy. The absence of these in other SNe Ia may reflect that the explosions have different progenitors: blueshifted Na I D features might be explained by the outflows of 'single-degenerate' systems (binaries of a white dwarf with a non-degenerate companion). In this work, we search for systematic differences among SNe Ia for which the Na I D characteristics have been clearly established in previous studies. We perform an analysis of the chemical abundances in the outer ejecta of 13 'spectroscopically normal' SNe Ia (five of which show blueshifted Na lines), modelling time series of photospheric spectra with a radiative-transfer code. We find only moderate differences between 'blueshifted-Na', 'redshifted-Na' and 'no-Na' SNe Ia, so that we can neither conclusively confirm a 'one-scenario' nor a 'two-scenario' theory for normal SNe Ia. Yet, some of the trends we see should be further studied using larger observed samples: Models for blueshifted-Na SNe tend to show higher photospheric velocities than no-Na SNe, corresponding to a higher opacity of the envelope. Consistently, blueshifted-Na SNe show hints of a somewhat larger iron-group content in the outer layers with respect to the no-Na subsample (and also to the redshifted-Na subsample). This agrees with earlier work where it was found that the light curves of no-Na SNe – often appearing in elliptical galaxies – are narrower, i.e. decline more rapidly.

Key words: supernovae: general – techniques: spectroscopic – radiative transfer

1 INTRODUCTION

Type Ia supernovae (SNe Ia) are one of the most well investigated but still poorly understood phenomena in astrophysics. The observed 'homogeneity' of the light curves of 'normal' SNe Ia (Hamuy et al. 1991; Branch et al. 1993; Phillips 1993; Goldhaber et al. 1998) enables cosmologists to use them as standardisable candles (cf. Phillips 1993; Phillips et al. 1999; Goldhaber et al. 2001; Takanashi et al. 2008). The resulting Hubble diagrams have led to the remarkable conclusion that the expansion of the Universe is accelerating (e.g. Riess et al. 1998; Schmidt et al. 1998; Perlmutter et al. 1999; Riess et al. 2007; Kessler et al. 2009; Sullivan et al. 2011).

Empirically, there are techniques to 'standardise' or 'calibrate' SNe Ia for cosmological purposes (i.e. to predict their luminosity) with relatively little scatter (e.g. Phillips et al. 1999; Guy et al. 2007; Jha et al. 2007; Takanashi et al. 2008; Wood-Vasey et al. 2008). However, SN cosmology and other fields of astronomy, being brought to new levels of accuracy, would require precise knowledge of the SN Ia explosion mechanism (cf. e.g. Foley et al. 2010), also predicting or excluding possible moderate drifts in the mean SN Ia properties with look-back time, such as changes in mean luminosity. Despite a great effort to understand SNe Ia, this knowledge is still lacking – it has been the matter of a long and ongoing debate (e.g. Hillebrandt & Niemeyer 2000; Greggio 2005; Howell 2011; Maoz et al. 2014) whether the bulk of SNe Ia emerge from single-degenerate systems (where one C/O white dwarf with an extended companion star explodes) or from double-degenerate systems (where two white dwarfs merge, collide or one is accreted onto the other). Furthermore, there are open questions on how exactly the thermonuclear flame ignites and propagates.

The models which have probably been most extensively tested in order to explain SNe Ia (for a review, see, e.g., Howell 2011) are (i) the 'single-degenerate-Chandrasekhar-mass' model (presumably a 'delayed detonation' of a C/O white dwarf before reaching its mass limit, i.e. the Chandrasekhar mass $M_{Ch} \sim 1.4\,M_\odot$), (ii) the 'double-detonation' sub-M_{Ch} model (a detonation of a less massive C/O white dwarf triggered by the detonation of an accreted helium shell), and (iii) the 'double-degenerate' model (merger of two C/O white dwarfs). Observations of SNe Ia in the UV, optical and IR have yielded constraints on the ejecta configuration and helped to demonstrate that recent explosion models may well explain the observed objects (e.g. Baron et al. 2006; Kasen et al. 2009; Sim et al. 2010; Kromer et al. 2013; Hachinger et al. 2013; Mazzali et al. 2014). However, only a few explosion models could definitely be excluded as for explaining normal SNe Ia [e.g. pure deflagrations within single-degenerate systems, which match peculiar, 2002cx-like SNe Ia (e.g. Branch et al. 2004; Sahu et al. 2008; Jordan et al. 2012; Kromer et al. 2013). Thus, a search for further observational characteristics for verifying or falsifying promising models has begun. A promising group of methods is focused on finding direct signatures of the progenitor systems (e.g. Patat et al. 2007; Gilfanov & Bogdán 2010; Shen et al. 2013; Silverman et al. 2013; Kerzendorf et al. 2014 – for a review, see Maoz et al. 2014).

One 'smoking gun' signature of the progenitor system could be narrow, Doppler-shifted Na I D absorption components from moving circumstellar material (CSM); see e.g. Patat et al. (2007); Simon et al. (2009); Blondin et al. (2009); Sternberg et al. (2011); Foley et al. (2012b); Maguire et al. (2013); Phillips et al. (2013); Ferretti et al. (2016). Na I D absorption components blueshifted with respect to the host galaxy indicate an outflow towards the observer – material which may have been ejected by the progenitor system. This may be most easily accommodated in the single-degenerate scenario (Patat et al. 2007, 2011; Booth et al. 2016; see, however, Phillips et al. 2013; Raskin & Kasen 2013; Shen et al. 2013; Soker 2014), with a recurrent-nova progenitor system. In observed samples of SNe Ia, one sees red- as well as blueshifted Na I D absorption systems, and many of these (e.g. Maeda et al. 2016) surely originate in the interstellar medium (ISM). However, samples of SNe Ia usually show more objects with blueshifted Na I D components than redshifted ones (e.g. Sternberg et al. 2011;

Foley et al. 2012b; Maguire et al. 2013) – suggesting[1] that some of the lines seen indeed have to do with the SN progenitors.

In this work, we test this idea, searching for differences in the mean physical properties of 'blueshifted-Na', 'single-' (not shifted, cf. Section 2) and 'redshifted-Na' SNe, and SNe with no hints of Na I D ('no-Na' SNe). We constrain ourselves to spectroscopically normal objects, and consider five blueshifted-Na, four redshifted-Na / single-Na and four no-Na SNe already classified (as for their CSM/ISM Na I D properties) by Sternberg et al. (2011); Foley et al. (2012b) and Maguire et al. (2013). The outer ejecta of these objects are analysed (i.e. the debris of the explosion – not the CSM/ISM) by modelling the spectral time series of the SNe with a well-tested radiative transfer code (Mazzali & Lucy 1993; Lucy 1999; Mazzali 2000; Stehle et al. 2005). Afterwards, we compare the mean ejecta properties we find among the different 'Na subsamples', focusing on the abundance structure of the explosion. In the abundances, we expect to possibly find differences from one Na subsample to another, just as those found between the single-degenerate delayed-detonation and double-degenerate violent-merger explosion models of Röpke et al. (2012). E.g., the mass in iron-group elements in the outer layers of these models (above $8000\,km\,s^{-1}$ in velocity space) differs by $0.3M_\odot$, while the total mass contained in these layers is practically equal ($\sim 0.9 M_\odot$).

Below (Section 2), we first discuss our data selection in the context of the idea of this work. We also give details on our methods including the modelling technique. Afterwards, we show example models in Section 3. In Section 4, the results for our entire sample are analysed. Finally, we draw conclusions (Section 5).

2   DATA SELECTION AND MODELLING

This section discusses the basis of our work. We first recap some important studies on narrow Na I D lines in high-resolution SN Ia spectra and illustrate what information high-resolution spectra provide in contrast to their low-resolution counterparts (Section 2.1). Afterwards, we describe our data sample and its treatment (Sections 2.2 & 2.3). Finally, we lay out our method to model time series of low-resolution spectra (Section 2.4).

2.1   High-resolution vs. low resolution spectra: Narrow Na I D vs. broad ejecta features

Spectra of SNe Ia show strongly Doppler-broadened features produced by the fast-expanding ejecta (velocities in the order of $10,000\,km\,s^{-1}$). These broad features can be analysed in low-resolution spectra. Their profiles (and the temporal evolution thereof) provide structural information about the SN material (composition, density, expansion velocities). On top of the 'intrinsic' SN features, higher-resolution spectra show narrow features (velocities of a few hundred $km\,s^{-1}$) due to the presence of CSM or ISM. These features can provide information on the configuration of the progenitor system and/or the host galaxy.

In a pioneering work, Patat et al. (2007) analysed the

---

[1] In addition, some of the objects exhibiting blueshifted Na I D absorption show a time variability of the absorption lines, which has been interpreted as evidence of the ionisation conditions being modulated by the nearby SN (Patat et al. 2007; Simon et al. 2009, but see e.g. Chugai 2008).
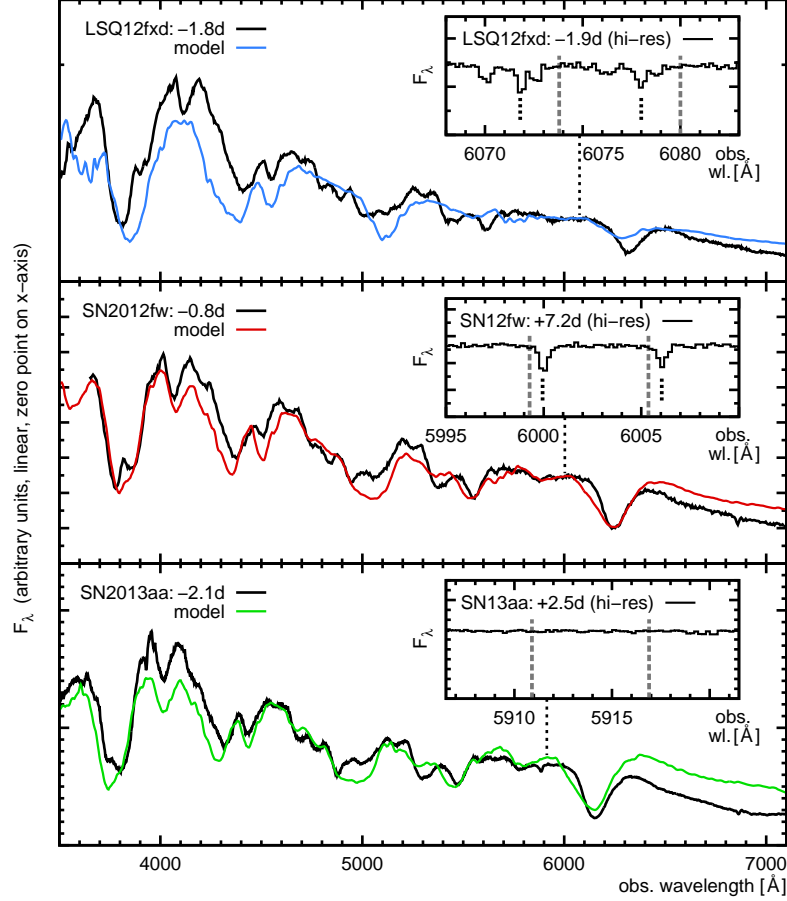
Figure 1. Typical spectra and models for SNe with blueshifted (LSQ 12fxd), redshifted (SN 2012fw) and absent (SN 2013aa) narrow Na I D lines. While e.g. Sternberg et al. (2011); Foley et al. (2012b); Maguire et al. (2013) and Phillips et al. (2013) have analysed Na I D and other ISM/CSM features to establish the ISM/CSM properties, we model low-resolution SN spectra with their strongly Doppler-broadened lines produced by the ejecta (main panels, black lines; model spectra: grey/coloured lines). In the insets, we show 15 Å wide regions of high-resolution spectra for the SNe. The data shown were analysed by Maguire et al. (2013) to examine the presence and possible wavelength shifts of narrow Na I D features (cf. their Figures 1, 2, 3). We have marked the expected SN-site rest-frame wavelengths for Na I D_1 and Na I D_2 with grey dashes, the actual wavelengths of the minima with black dots.

CSM/ISM Na I D lines[2] of SN 2006X in a time series of high-resolution spectra. They found that some CSM/ISM Na I D components are blueshifted with respect to the rest frame of the SN, and that the strength of these components changes with time, which they interpreted as being caused by an ionisation effect from the SN [for a theoretical assessment of this, and possible caveats, see e.g. Chugai (2008) and Booth et al. (2016)]. Estimating the properties of the CSM (extent, hydrogen mass, etc.), they concluded that the material may have originated from nova outbursts in a single-degenerate progenitor system. The variable-Na I D phenomenon was later found to be present in more SN Ia spectra (e.g. Simon et al. 2009; Blondin et al. 2009; Stritzinger et al. 2010).

Na I D properties in larger samples of SNe Ia have also been systematically analysed (Sternberg et al. 2011; Foley et al. 2012b; Maguire et al. 2013; Phillips et al. 2013). These studies support the hypothesis that the lines sometimes arise from CSM. Sternberg et al. (2011) reported an excess of SNe Ia showing

blueshifted compared to redshifted Na I D features with respect to the SN rest frame. This suggests that the material generating the features shows a preference of moving from the SN towards the observer. ISM clouds not related to the progenitor system would move randomly. Using larger samples of SNe Ia, Foley et al. (2012b) and Maguire et al. (2013) confirmed this result. These studies also investigated correlations between Na I D properties and SN properties (luminosity, expansion velocities, etc.) and found various possible hints the existence of two progenitor populations (one of them preferentially producing blueshifted-Na SNe Ia). Phillips et al. (2013) found that SNe with blueshifted Na I D tend to deviate from the normal correlation between ISM Na I D column densities and the dust extinction (reddening). They show 'too strong' Na I D lines for 'too little' extinction, suggesting that the material is CSM with a composition different from average ISM.

In this work, we perform a structural analysis of a SN Ia sample for which the properties of their Na I D have previously been measured in moderate- and high-resolution spectra. To this purpose, we model the 'intrinsic' SN features in time-series of spectra with a radiative-transfer code. This enables us to quantify differences in the structure of the SNe Ia linked to the presence or absence of blueshifted Na I D absorption features. For our models reproducing the broad 'intrinsic' SN features and their

---

[2] The studies on Na I D mentioned here also analyse different (often weaker) CSM/ISM features like Ca II H & K or K I λλ7665, 7699. In our study, we concentrate on the Na I D information available for a relatively large number of objects.

time evolution, it is sufficient to use low-resolution spectra (which have the advantage of well-sampled time series being available for many objects). Figure 1 illustrates what information we extract from low-resolution spectra (main panels) as opposed to what the studies on Na I D extract from high-resolution data (inserts). The Figure shows three example objects analysed in this work (LSQ 12fxd, SN 2012fw and SN 2013aa), which show different Na I D behaviours. Overplotted on the low-resolution SN spectra, we show our models discussed below (Sections 2.4 and 3). With the models, we aim at reproducing not only the data shown in the main panels of Figure 1, but the entire spectral time series of each SN around maximum light, inferring the ejecta characteristics (Section 2.4).

2.2   SN sample

2.2.1   Sample selection

As a basis for our study, we have considered SNe Ia for which the presence of blue-/redshifted narrow Na I D components has been measured using intermediate- or high-resolution spectra by Sternberg et al. (2011); Foley et al. (2012b) and Maguire et al. (2013). We selected 13 objects for our final modelling work (see Table 1), demanding that the objects have an unambiguous classification of the Na I D central wavelength shift, that a sufficient set of flux-calibrated low-resolution photospheric spectra is available (i.e. usually a minimum of four spectra, with at least two of them before maximum light), and that they are considered 'normal' SNe Ia (e.g. Branch et al. 1993; Filippenko 1997; Leibundgut 2000). Therefore, we have, e.g., excluded the SNe 1986G [strongly reddened, subluminous with Ti II lines – Cristiani et al. (1992), Phillips et al. (1987), Ashall et al. (2016b)], 2006X [strongly reddened, high line velocities – Wang et al. (2008); Yamanaka et al. (2009)], 2009ig [extremely high line velocities – Foley et al. (2012a)] and LSQ12gdj [1991T-like – Scalzo et al. (2014); cf. also Phillips et al. (1992); Jeffery et al. (1992)]. We have also refrained from modelling PTF 11kx (Dilday et al. 2012), for which time-variable Na I D lines as well as other signs of CSM interaction have been found, but which shows a quite unusual spectrum almost without S II $\lambda\lambda$5454,5640 after B maximum. We note that, although we chose to concentrate on normal SNe Ia in this work, modelling peculiar objects will be an interesting subject for forthcoming studies.

2.2.2   Division of our sample into 'Na subsamples'

We group our SNe Ia, following Sternberg et al. (2011), into four classes ('Na subsamples', see also Table 1):

- 'blueshifted-Na' objects,
- 'redshifted-Na' objects,
- one 'single-Na' object,
- and 'no-Na' objects.

In our terms, a 'SN with blue-/redshifted Na' is an object with narrow Na I D absorption components blue-/redshifted with respect to the host-galaxy Na I D wavelength, where these SNe usually show their strongest narrow Na I D absorption component. 'No-Na' objects show no Na I D line at all, while the 'single-Na' object shows only one strong component at the host-galaxy Na I D wavelength.

Maguire et al. (2013) modified the classification scheme of Sternberg et al. (2011), by (i) measuring the blue-/redshift of the features with respect to an independently confirmed host-galaxy rest wavelength (obtained from sources other than the strongest

Na I D component), and (ii) statistically grouping the SNe into objects with blueshifted Na I D components ('blueshifted-Na I D' SNe – regardless of redshifted components in their work), objects without blueshifted Na I D components ('non-blueshifted-Na I D' SNe) and objects without any Na I D ('no-Na I D' SNe). The SNe with blue- or redshifted Na we model in our work have shown *no significant evidence* for a Na I D component of the respective other sort. We have selected objects which, apart from rare cases (see remarks in Table 1), are part of the respective class regardless of the classification method (Sternberg et al. 2011; Maguire et al. 2013).

2.3   Data handling

The photospheric spectra we use for the ejecta modelling have mostly been obtained within larger campaigns, such as the CFA SN follow-up (Blondin et al. 2012), the PESSTO[3] survey (Smartt et al. 2015), the Berkeley Supernova Ia program BSNIP (Silverman et al. 2012), and the European SN Collaboration (EU RTN HPRN-CT-2002-00303). Table 1 lists the precise sources for the spectra object by object. Most of the data are publically available through the WISeREP repository[4] (Yaron & Gal-Yam 2012), and the PESSTO spectra are available through the ESO archive (see PESSTO web pages for details). The absolute calibration of the observed spectra has then been checked against photometry [from light-curve samples of Hicken et al. (2009), Ganeshalingam et al. (2010), Stritzinger et al. (2011), Brown et al. (2012) and the papers cited in Table 1] using IRAF/SYNPHOT. In case deviations were found, the spectra affected were multiplied by a suitable polynomial function $f(\lambda)$ of degree $\leqslant 2$ (with only a mild variation of $f(\lambda)$ with wavelength), respectively, such that the resulting sample of spectra is consistently flux-calibrated.

While we apply no reddening correction (correction for dust extinction) to the observed spectra, our spectral models are artificially reddened using a total extinction estimate (see Table 1). The host-galaxy reddening is often subject to considerable uncertainty, especially in cases where we could only estimate the reddening from Na ID line depths [Turatto et al. (2003); see Phillips et al. (2013) and Poznanski et al. (2011) for caveats]. Resulting uncertainties in our models are mitigated by the fact that we do not model highly reddened SNe Ia.

2.4   Modelling method

In order to analyse the photospheric spectra of our SN sample and derive ejecta properties, we use the abundance reconstruction method of Stehle et al. (2005). A modelling of nebular spectra and bolometric light curves, which is part of their 'Abundance Tomography' approach, is not performed in this work, as for a number of our objects the respective data are not available.

For modelling the photospheric spectra, we use a well-tested Monte-Carlo radiative transfer code (Lucy 1999; Mazzali 2000; Stehle et al. 2005; for a short description see e.g. Mazzali et al. 2014) which calculates a synthetic spectrum from a given bolometric luminosity $L_{\rm bol}$, time from explosion t, photosphere position/velocity[5] $v_{\rm ph}$, density profile $\rho(v)$, and abundance stratifica-

---

[3] http://www.pessto.org
[4] http://www.weizmann.ac.il/astrophysics/wiserep/
[5] Owing to the homologous expansion of the ejecta setting in seconds to minutes after the explosion of a SN Ia (e.g. Röpke 2005), v and r can be used interchangeably at any given point of time t ($r = v \times t$).

Table 1. SNe grouped into the different subsamples. For each object we give $\Delta m_{15}(B)$, total extinction [for our moderate-redshift SNe: sum of the galactic and host-galaxy extinction values, $E(B-V)_{\text{tot.}} = E(B-V)_{\text{MW}} + E(B-V)_{\text{host}}$] and SN redshift ($z$) values assumed in the modelling process, and sources of the respective spectra.

Object	$\Delta m_{15}(B)^{a,c}$	$E(B-V)_{\text{tot.}}^{b,c}$	host type^c	z^c	references spectra	remarks
			Blueshifted Na (no redshifted Na)			
SN 2002bo	1.2	0.38	Sa	0.004	Benetti et al. (2004)	Already modelled by Stehle et al. (2005); re-modelled according to the rules in Section 2.4.
SN 2002ha^c	1.2	0.23	Sab	0.014	Blondin et al. (2012)	Calculated $E(B-V)_{\text{host}}$ of 0.14 from narrow Na I D equivalent width^d using the lower-limit relation of Turatto et al. (2003).
SN 2007le	1.0	0.22^e	Sc	0.007	Blondin et al. (2012)	
SN 2008ec	1.1	0.21	Sa	0.016	Silverman et al. (2012)/ Milne et al. (2013)	Assumed $E(B-V)_{\text{host}}$ value calculated by Milne et al. (2013) from the peak photometry.
LSQ 12fxd^f	0.8^h	0.08	Sc	0.031	Maguire et al. (2013)/ PESSTO	Inferred host extinction of 0.06 from Na I D equivalent width^d (see SN 2002ha; here: lower limit of various spectra.
			Redshifted Na (no blueshifted Na)			
SN 2001el^c	1.2	0.22	Scd	0.003	Wang et al. (2003); Mattila et al. (2005); Krisciunas et al. (2003)	
SN 2012fw^g	0.8^h	0.07	S0/a	0.019	Maguire et al. (2013)/ PESSTO	Inferred host extinction of 0.04 from Na I D equivalent width^d (see SN 2002ha).
SN 2012hr	1.0^h	0.05	Sbc	0.007	Maguire et al. (2013)/ PESSTO	Inferred host extinction of 0.01 from Na I D equivalent width^d (see SN 2002ha).
			Single (host-wavelength) Na			
SN 2002cr^c	1.2	0.08	Scd	0.009	Blondin et al. (2012)	Inferred host extinction of 0.06 from Na I D equivalent width^d (see SN 2002ha).
			No Na			
SNF 20080514-002	1.4	0.03	S0	0.022	Blondin et al. (2012)/ Brown et al. (2012)	
LSQ 12dbr	0.9^h	0.06	Irr	0.020	Maguire et al. (2013)/ PESSTO	Assumed negligible host extinction because of absence of narrow Na I D.
SN 2012ht	1.4	0.03	Irr	0.004	Maguire et al. (2013)/ PESSTO/ Tomasella et al. (2014)^i/ Yamanaka et al. (2014)	Host extinction negligible (Yamanaka et al. 2014).
SN 2013aa	0.8^h	0.15	Sc	0.004	Maguire et al. (2013)/ PESSTO/ T. Bohlsen^j	Assumed negligible host extinction because of absence of narrow Na I D.

^{a} Reddening-free B-band decline within 15 d directly after B maximum (Phillips et al. 1999).

^{b} Total dust extinction – extinction within the host galaxy and the milky way can be added for low-redshift objects to obtain a total extinction $E(B-V)_{\text{tot.}}$.

^{c} Basic data [$\Delta m_{15}(B)$, $E(B-V)$, host type, z] for the SNe have been taken from Maguire et al. (2013), Foley et al. (2012b), Sternberg et al. (2011) and the cited papers for each SN, unless noted otherwise.

^{d} To the purpose of applying the relation of Turatto et al. (2003), which approximates the extinction based on narrow Na I D features as seen in *low-resolution* data, we measured the equivalent width of the narrow Na I D feature at the host-galaxy rest wavelength in our low-resolution spectra whenever the line was measurable (including Na I D components which may be due to the SN progenitor – also this dust will redden the SN) and took the average. The uncertainty in the reddening introduced here has no major impact on our results, as all objects affected are relatively weakly reddened.

^{e} From Simon et al. (2009) – in their work, $E(B-V)_{\text{tot.}} = 0.27$ with $R_V = 2.59$. For consistence with the other SNe, we assume $R_V = 3.1$ and a lower reddening of $E(B-V)_{\text{tot.}} = 0.22$, for which our reddening law best reproduces the A_B and A_V values of Simon et al. (2009) (with the same error each).

^{f} LSQ 12fxd, with respect to the strongest Na I D component, displays a blueshifted component as well as a redshifted component (slightly weaker and attached to the strongest component). It may thus have been classified as 'symmetric' by Sternberg et al. (2011).

^{g} SN 2012fw displays only one strong Na I D line extended somewhat more to the red. Sternberg et al. (2011) may thus have classified it as 'symmetric'.

^{h} Calculated from the stretch values of Maguire et al. (2013), using equation (5) of Conley et al. (2008).

^{i} The spectrum used is the classification spectrum reported by Ochner et al. (2012).

^{j} Amateur spectrum of 16 Feb. 2013 downloaded (at 03 Jun. 2014) from `http://users.northnet.com.au/~bohlsen/Nova/sn_2013aa.htm`.
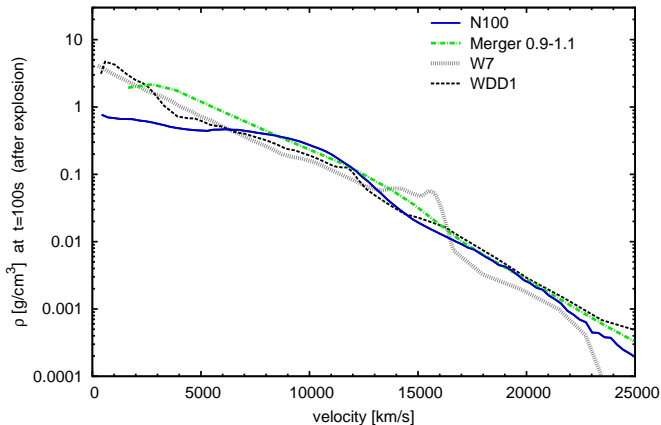
Figure 2. The N100 density profile (Seitenzahl et al. 2013) used as input data for our radiative transfer calculations (dark (blue), solid line). For comparison, we show the density of a WD merger [$0.9 M_\odot$ and $1.1 M_\odot$ C/O white dwarfs, Pakmor et al. (2012) and Röpke et al. (2012) – light (green), dashed-dotted line]. We furthermore show models of Nomoto et al. (1984); Iwamoto et al. (1999) – W7 (1D fast deflagration – grey, broad/micro-dashed line) and WDD1 (1D delayed detonation – black, dashed line), which have been used in many previous spectral modelling studies.

tion $\mathbf{X}(v)$ (where $\mathbf{X}$ is the tuple of mass fractions of all relevant elements).

To keep the parameter space for the models small enough to be thoroughly explored, t and $\rho(v)$ follow a fixed parametrisation. The luminosity $L_{\rm bol}$, some of the abundances $\mathbf{X}(v)$, and the photospheric velocity $v_{\rm ph}$ are used as fitting parameters, which we optimise to match the observed spectra. In this fitting process, we infer a best-fit abundance stratification, from which we can assess differences between the observed SNe in terms of the chemical structure.

Before proceeding with the presentation of the models, we shortly discuss how we set the 'fixed' code input parameters, and how we adjust the 'free' input parameters when fitting an actual spectral sequence.

2.4.1 Fixed parameters

We use the spherically averaged density from the relatively recently published N100 three-dimensional delayed-detonation model (Figure 2) of Seitenzahl et al. (2013) as a fixed input density profile $\rho(v)$ reasonably representing SNe Ia. As Seitenzahl et al. (2013) mention, out of their suite of explosion models, this model best matches the ^{56}Ni production of typical SNe Ia [$\sim 0.6 M_\odot$, Stritzinger et al. (2006)]. Uncertainties in state-of-the-art explosion simulations (such as the unknown number and geometry of ignition points in Chandrasekhar-mass models), and the open question of the 'typical' explosion scenario(s), clearly translate to some degree of uncertainty in our models. In order to give the reader a feeling for these uncertainties, we compare (Figure 2) the N100 density profile to that of the 'classical' W7 and WDD1 single-degenerate explosion models (Nomoto et al. 1984; Iwamoto et al. 1999), and to the density profile of a spherically averaged white dwarf merger [$0.9 M_\odot$ and $1.1 M_\odot$ C/O white dwarfs, Pakmor et al. (2012) and Röpke et al. (2012)]. It is clear that the differences between the density profiles are significant, but not extreme in the region where photospheric spectra around maximum light form ($\sim 5000 – 25000\,{\rm km\,s^{-1}}$). The mass above $8000\,{\rm km\,s^{-1}}$, the velocity down to which we analyse the ejecta (see Sec. 3.1 below), is almost equal in both models. Thus, we do not expect our results

to depend much on the density profile used. We demonstrate this with an explicit test – a repetition of our modelling with the merger density profile from Röpke et al. (2012) – in Appendix A.

Having set the density profile in velocity space, the second input parameter to be fixed is the time from explosion onset to the epoch of a certain observed spectrum (where the latter is normally given with respect to B-band maximum by the observers). The time from explosion is calculated as

$$t = t_{\rm obs.} + t_r$$

where $t_{\rm obs.}$ is the observationally-determined time offset from B-band maximum, and t_r is the B-band rise time which we calculate approximately as:

$$t_r = 18.9\,{\rm d} - 2.0\,{\rm d} \times \left(\frac{\Delta m_{15}(B)}{\rm mag} - 1.17 \right).$$

We have chosen this formula as a linear approximation to the rise time in $\Delta m_{15}(B)$ [the B-band light-curve decline during the first $15\,{\rm d}$ directly after B maximum, Phillips (1993)], assuming that SNe Ia with a faster decline also rise faster because of a smaller opacity. The parameters in the formula are tuned to obtain a rise time of $18.9\,{\rm d}$ for SN 2002bo with $\Delta m_{15}(B) = 1.17$ (i.e. to reproduce the values of Benetti et al. 2004) and to obtain a rise-time range of $\pm 1\,{\rm d}$ for our SN sample (as given in Table 1). This roughly corresponds to the spread found in light-curve samples of normal SNe Ia (e.g. Conley et al. 2006; Strovink 2007; Ganeshalingam et al. 2011; Firth et al. 2015).

2.4.2 Fitting parameters and fitting procedure

Using the approach of Stehle et al. (2005), the radial abundance stratification is reconstructed from the outside inwards. We begin to optimise the abundances starting from typical 'default' values similar to those inferred for SN 2002bo (Stehle et al. 2005). For a more detailed description of the procedure, we refer to their original paper, but here we give at least a basic explanation.

To begin with, the earliest spectrum available for a respective SN is fit optimising the abundances in two separate zones (cf. Hachinger et al. 2013)[6]. One zone lies between the very outside of the simulated atmosphere (where negligible densities are reached, $v \sim 40000\,{\rm km\,s^{-1}}$) and $20000\,{\rm km\,s^{-1}}$ – in this zone, we assume a very weakly burned composition, with Fe-group elements only at the solar-metallicity level remaining from the progenitor (the exact metallicity level is irrelevant here, as we do not model the UV). The second zone in which we optimise the abundances is between $20000\,{\rm km\,s^{-1}}$ and the photospheric velocity $v_{\rm ph}$ at the epoch of the first available spectrum. This photospheric velocity, let us call it 'v_1', is determined such that the overall opacity of the atmosphere is reasonable, line velocities are matched and the overall colour of the observed spectrum can be reproduced. The luminosity $L_{\rm bol}$ is determined such that the overall flux level in the observed spectrum is matched by the synthetic spectrum. This quantity, together with the photospheric velocity $v_{\rm ph}$ and the iron-group abundances largely determines the temperature structure within the model atmosphere. Thus, when any of these three parameters is changed, usually the abundance structure has to be somewhat re-adjusted so as to keep an optimum fit.

---

[6] In Hachinger et al. (2013), three separate zones were used as sufficient early-time data were available to avoid parameter degeneracies in the fitting process.

Table 2. Prototypical abundance zones for our spectral models with their respective adjustable (i.e. fitted within the given limits) and fixed abundances. The fixed abundances in zones I-VII (given to one significant digit for simplicity) are derived from the spatially-averaged nucleosynthesis of the N100 model (Seitenzahl et al. 2013) in different radial layers. Models other than N100 (e.g. Iwamoto et al. 1999; Gamezo et al. 2005) have somewhat different chemical yields; however, qualitatively, the composition patterns remain similar. In each zone of our models, the abundances are chosen such that the spectra are optimally fit, *under the constraint (see also text)* that the abundance pattern must match one of the zone patterns I-VII. Elements not mentioned are not unambiguously seen in the spectrum and are assumed not to be present (zero abundance). 'Solar' abundances have been taken from Asplund et al. (2009).

zone	I	II	III	IV	V	VI	VII
corresponding v range in N100 [km s^{-1}]	< 6000	$6000 - 12000$	$12000 - 13500$	$13500 - 15000$	$15000 - 17000$	$17000 - 20000$	> 20000
fitted abundances; respective constraints for adjustment (if one abundance value is given: abundance fixed in respective zone)							
$X(C)$ [mass fraction, %]	0.0^a	0.0^a	0.0^a	0.0^a	$\leqslant 0.3$	$\leqslant 3.0$	12.0
$X(Si)$ [mass fraction, %]	adjusted such that	$\sum_i X(i) = 100\%$	$30.0 - 40.0$	40.0	40.0	$\leqslant 30.0$	5.0 or 1.0^b
$X(Ca)^c$ [mass fraction, %]	0.0^a	$\leqslant 5.0$	$\leqslant 5.0$	$\leqslant 5.0$	$\leqslant 5.0$	$\leqslant 5.0$	$\leqslant 1.0$
$X(Fe_0)^d$ [mass fr., %]	3.0	10.0	7.0	$1.0 - 5.0$	$0.1 - 1.0$	solar	solar
$X(^{56}Ni_0)^d$ [mass fr., %]	70.0	$30.0 - 60.0$	$5.0 - 30.0$	$= X(Fe_0)$	$= X(Fe_0)/2$	$\leqslant X(Fe_0)/10$	0.0
fixed abundances							
$X(O)$ [mass fraction, %]	0.0^a	0.0^a	–	adjusted such that	$\sum_i X(i) = 100\%$	–	
$X(Mg)$ [mass fraction, %]	0.0^a	0.0^a	0.0^a	1.0	4.0	9.0	$= X(Si)$
$X(S)$ [mass fraction, %]	$= X(Si)/2$	$= X(Si)/2$	$= X(Si)/3$	$= X(Si)/3$	$= X(Si)/4$	$= X(Si)/4$	$= X(Si)/5$
$X(Ti)$ [mass fraction, %]	0.001	0.002	0.003	0.007	0.005	0.001	solar
$X(V)$ [mass fraction, %]	0.0300	0.0400	0.0200	0.0020	0.0001	solar	solar
$X(Cr)$ [mass fraction, %]	0.70	0.70	0.20	0.10	0.02	solar	solar

[a] Set to 0.0 because abundance in this zone is too small to have an influence on synthetic spectra and integrated abundances.

[b] 5.0% when the early Si line of the SN extends to high velocities (blueshifts) indicating the presence of burning products at high velocity; 1.0% otherwise.

[c] Ca abundances are chosen larger than in the N100 model (cf. Seitenzahl et al. 2013), as otherwise the Ca lines in the spectra could not be well fitted. This problem may arise from uncertainties in the Ca atomic data for radiative transfer as well as in the exact nucleosynthesis; Ca abundances are not of major relevance for our further analysis in any case.

[d] The abundances of Fe, Co and Ni in our models are assumed to be the sum of ^{56}Ni and its decay chain products (^{56}Co and ^{56}Fe) on the one hand, and directly synthesised / progenitor Fe on the other hand (other contributions are can be neglected for spectral synthesis). Thus, they are conveniently given in terms of the ^{56}Ni mass fraction at $t = 0$ [$X(^{56}Ni)_0$], the Fe abundance at $t = 0$ [$X(Fe)_0$], and the time from explosion onset t.

After matching the first spectrum, the fitting process is continued by finding abundances, L_{bol} and v_{ph} for the second spectrum. The new photospheric velocity, v_2, will be lower, corresponding to the recession of the photosphere into the intermediate ejecta with time. The abundances are then only fit between v_1 and v_2, while the values in the layers above v_1 are taken as given and remain fixed[7]. This process is continued with later and later spectra (to determine the abundances between v_2 and v_3, and so on); we stop when we have modelled a spectrum $5 - 10$ days after maximum. At this point, the photosphere has usually receded into zones rich in ^{56}Ni, and the assumption that all radiation is generated below an assumed photosphere (which is implied by our modelling approach) becomes much less accurate.

As we model a large number of objects in the present study, we speed up the fitting process narrowing down the parameter space by only allowing abundance combinations 'typical' for certain 'burning zones' in the hydrodynamics/nucleosynthesis model N100 (Seitenzahl et al. 2013). We note that 3D delayed-detonation explosion models like N100 do not exhibit the strictly-layered nucleosynthesis structure found in 1D simulations (Thielemann et al. 1986). Instead, material burnt in the initial deflagration rises convectively; the strength of the deflagration and thus the 'mixing' will depend on the somewhat uncertain ignition conditions. Finally, the deflagration turns into a detonation and practically the entire pre-expanded star undergoes nuclear reprocessing (Seitenzahl et al. 2013). Despite all uncertainties, in Table 2 we give a very approximate division of the ejecta of N100 into different zones with typical abundance patterns. Each abundance-fitting zone in our models (corresponding to a spectrum) is assigned the best-matching such zone, for which some abundances are considered fixed, and the others adjustable within limits (Table 2). In the deepest layers of N100 ($v < 6000$ km s^{-1}), material burnt to nuclear statistical equilibrium (NSE) dominates – mostly ^{56}Ni [more neutron-rich material such as ^{54}Fe is also produced, but partly ejected at higher velocities (Seitenzahl et al. 2013)]. Above this ejecta core, a zone with a very 'mixed' composition is found; Fe-group elements are still dominant in the inner part of this zone, but intermediate-mass elements (IME such as Si and S, $8 < Z \leqslant 20$) dominate at

[7] An exception to this can be abundances which at an early epoch are not well determined because of degeneracies (e.g. when two elements contribute to the same feature in the spectrum) or which only have moderate influences on the early-epoch fit. When the abundances chosen then prove incompatible with a later spectrum (effectively lifting the degeneracy), they are revised such as to fit all spectra in the time series equally well.

its outer edge ($v \sim 12000\,\mathrm{km\,s^{-1}}$). Going still further outwards, zones dominated by IME follow, and above $17000\,\mathrm{km\,s^{-1}}$, finally O dominates as a burning product. The outermost envelope above $\sim 20000\,\mathrm{km\,s^{-1}}$ is very weakly burned – a feature directly implemented in our models.

3   MODELS

Having laid out the modelling method, we discuss our model for SN 2007le (see Table 1) as an example. This object is a representative 'normal' SN Ia ($\Delta m_{15}(B) = 1.0$; no spectroscopic peculiarities), for which a series of (low-resolution) spectra with decent time coverage for the abundance analysis is available. High-resolution spectra of the object have revealed a blueshifted Na I D component (Sternberg et al. 2011). We first present the spectral fits and then discuss the abundance structure of the optimum-fit model.

Our model spectra and abundance structure plots for all other SNe from Table 1 can be downloaded as *supplementary online material (part A)* to this paper on the MNRAS web site. Basic information on the models (luminosities, photospheric velocities, etc.) is included.

3.1   Fits to the spectral sequence

The spectral sequence for SN 2007le which we have modelled (Figure 3) comprises six spectra from $-10.4\,\mathrm{d}$ to $+9.6\,\mathrm{d}$ (relative to B maximum). This constitutes a fairly typical case with respect to epoch coverage, although there is a large gap (between $-6.5\,\mathrm{d}$ and $+5.5\,\mathrm{d}$) around B maximum. To reach a sufficient accuracy in the reconstruction of the abundance profile of SN 2007le, we fit three spectra at comparatively late epochs, which mitigates – at least to a sufficient degree – the uncertainties in abundance reconstruction caused by the gap.

Figure 3 shows the time sequence of models and observed spectra; in the top panel, we have given line identifications for a typical pre-maximum spectrum as we use it in our study. These line identifications are (to good approximation) valid for all our models; only some ten days after B maximum, the main contributions to the features change, which reflects in changes in the spectral shape (see also e.g. Stehle et al. 2005).

At the earliest two epochs, the model fits are very good, except for typical problems reproducing the extreme blue wings of the strongest lines (Ca H&K, Si II $\lambda 6355$). These absorption wings, so-called high-velocity features (HVF; e.g. Mazzali et al. 2005, Childress et al. 2014), are supposedly caused by an enhanced electron density in the outermost ejecta, the cause of which may be a density bump or mixing of the ejecta with H-rich material lost by the progenitor system (cf. Tanaka et al. 2008). In any case, this material has a small net mass (such that it does not contribute significantly to integrated abundances) and – apart from the formation of the high-velocity components – also a small influence on the spectrum. We thus merely ignore it in our study here.

The fits to the pre-maximum spectra allow for a robust abundance diagnosis of the IME-dominated outer ejecta (cf. line identifications in Figure 3). The features dominated by Ca, Mg, S, Si and Fe lines are fit well overall. Some deficit of flux around $\sim 4000\,\text{Å}$ may be attributed to a weak re-emission part of the Ca II H&K P-Cygni profile in the model (corresponding to the missing high-velocity absorption). The mixed Fe II/Fe III/Mg II absorption trough around $4300\,\text{Å}$ is somewhat too shallow, probably owing to

the low Mg mass fractions we use following the explosion models (Table 2). These problems are not expected to significantly affect our analysis in Section 4, where we consider only major abundances (Fe-group, Si, O).

Our analysis is expected to be sufficiently reliable down to a velocity of $\sim 8000\,\mathrm{km\,s^{-1}}$, where the abundances of iron-group elements increase in most SNe. Such a photospheric velocity is expected shortly after B maximum. In mass space, the region analysed corresponds to $0.9\,\mathrm{M_\odot}$ of material (assuming the N100 density profile). The remaining core can only be well analysed using nebular spectra (e.g. Kozma et al. 2005; Mazzali et al. 2007). Correspondingly, after maximum light (Figure 3, lowermost three panels) the fit quality degrades somewhat. Some lines are too deep in the models (especially S II $\lambda 5640$ – here, part of the mismatch may be due to relatively large S abundances assumed following N100, see Table 2), and beyond $\sim 6500\,\text{Å}$, the model spectra show some flux excess. The latter is expected when assuming all energy generation to happen below a sharp photosphere and the photosphere to emit a black body (cf. Stehle et al. 2005; Hachinger et al. 2013). Spectra later than a few days after B maximum are therefore mainly useful as a rough consistency check, showing whether the best-fit composition found for the outermost layers is compatible with all data available.

3.2   Abundances

The abundances we find for SN 2007le down to $8000\,\mathrm{km\,s^{-1}}$ are shown in Figure 4, together with the chemical structure obtained in the N100 simulation (Seitenzahl et al. 2013), which can be considered a normally luminous 'standard' SN Ia model.

It is evident that SN 2007le does not show a ^{56}Ni distribution extending as much out as in N100; this seems to be replaced by intermediate-mass elements. Therefore, the total mass of ^{56}Ni in our model – even if assuming a ^{56}Ni-dominated core – is $\lesssim 0.4\,\mathrm{M_\odot}$, corresponding to a sub-luminous explosion with a bolometric luminosity of $\log\left(\frac{L}{\mathrm{L_\odot}}\right) \lesssim 9.3$ (equation 1 of Stritzinger et al. 2006). This is plausible, given that our models some days before/after maximum light (Figure 3) have a luminosity of $\log\left(\frac{L}{\mathrm{L_\odot}}\right) = 9.2$ (with the spectral flux scale checked to the best of our knowledge), and that typical SNe Ia show a luminosity variation of about 0.1 dex in this period (e.g. Pastorello et al. 2007).

The reason why SN 2007le has shown a slow light-curve decline [$\Delta m_{15}(B) = 1.0$, Table 1] for such a low-luminosity object is not exactly clear. We speculate, however, that the relatively flat abundance gradients in the SN (implying that IME and NSE elements are found up to the very outer layers) may favour photon trapping inside the envelope and thus slow down the evolution of the light curve (cf. Mazzali & Podsiadlowski 2006).

4   ANALYSIS AND DISCUSSION

In this section, we quantitatively compare models for SNe with blueshifted Na I D lines to models for other SNe. First, we evaluate photospheric velocities in the models (Section 4.1), which give hints about the overall opacity of the envelope (which, in turn, correlates with the composition). Afterwards, we show the integrated chemical yields of major species (Fe-group, Si, O) in the layers modelled (Sections 4.2 and 4.3). We conclude with a discussion of our findings in the context of the SN Ia progenitor problem (Section 4.4).
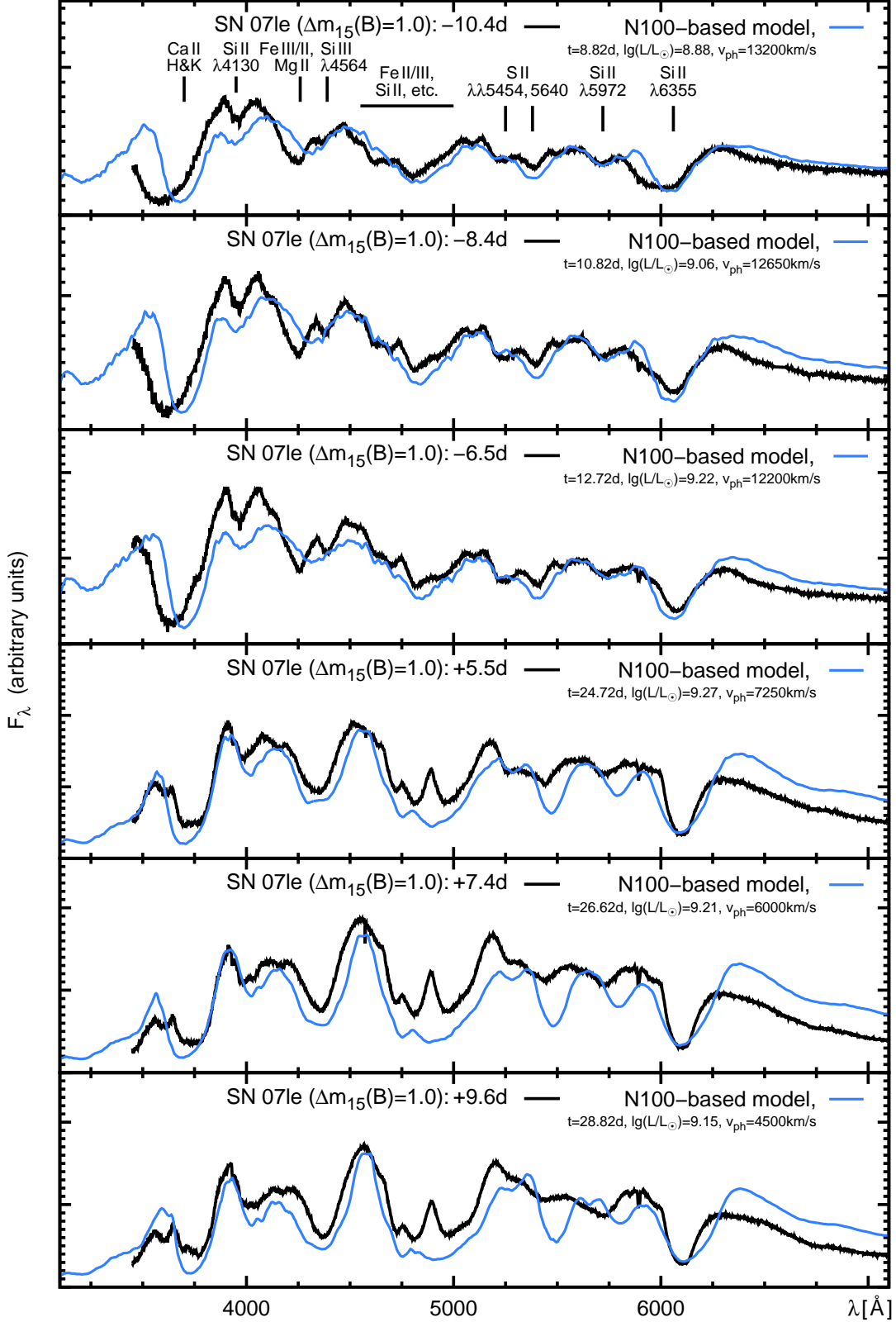
Figure 3. Model sequence for SN 2007le (blue lines). The observed (low-resolution) spectra (black lines) are plotted for comparison; line identifications are given for the most prominent features in the earliest spectrum. Observations and models are shown de-redshifted (i.e. in the SN's rest frame); no correction for reddening has, however, been applied to the observed spectra [the models have thus been reddened by $E(B-V)_{\text{total}} = 0.22$ mag, applying a CCM extinction law with $R_V = 3.1$ (Cardelli et al. 1989)].
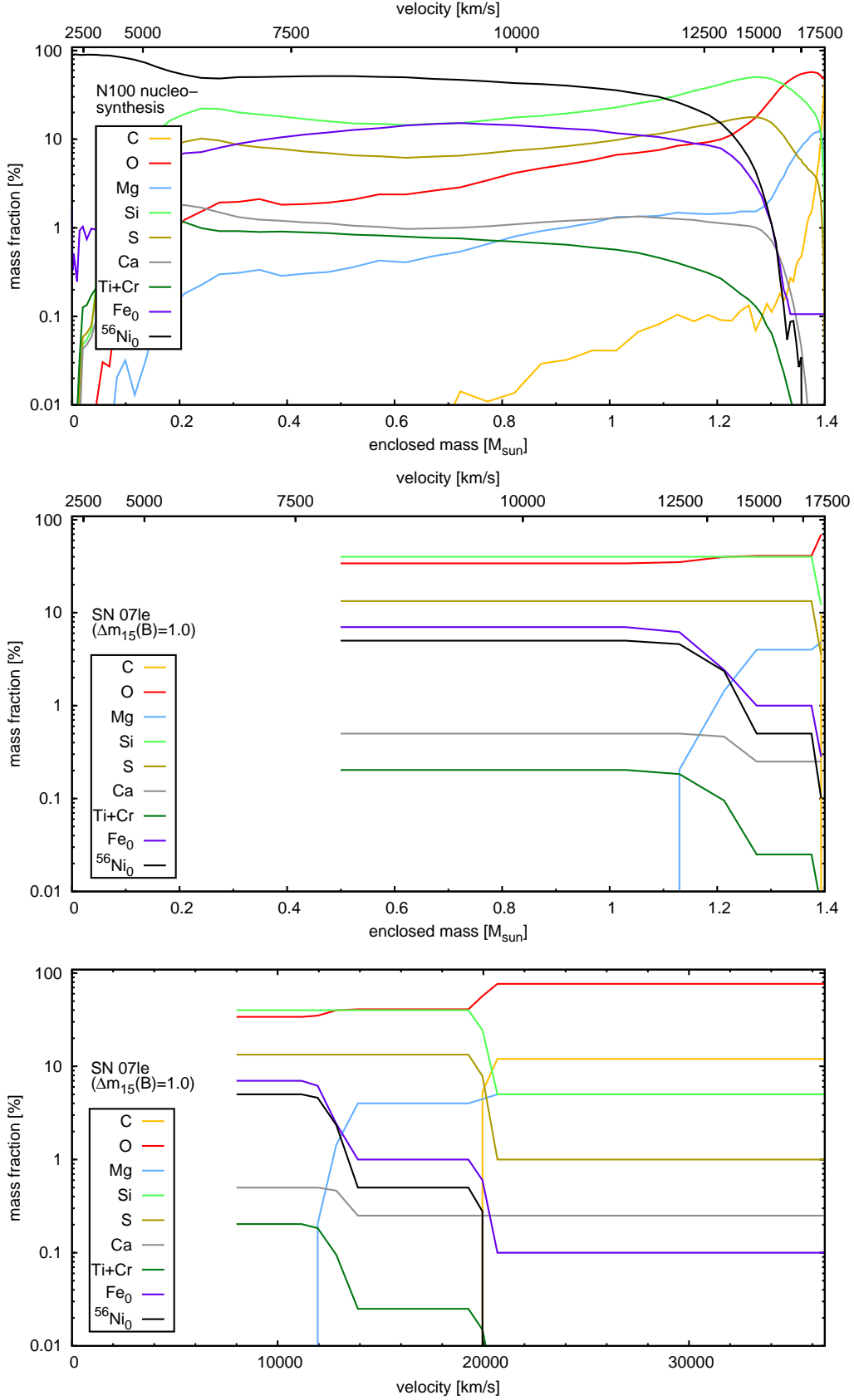
Figure 4. Abundance structure of N100 nucleosynthesis calculations (Seitenzahl et al. 2013, *top panel*, plotted in mass space), compared to our tomography of SN 2007le based on the N100 density profile (*middle panel*: in mass space; *lower panel*: in velocity space). The Ni/Co/Fe abundances are given in terms of the mass fractions of ^{56}Ni and stable Fe at $t = 0$ [$X(^{56}\text{Ni}_0)$, $X(\text{Fe}_0)$]; in our spectral models, no stable Ni or Co and no radioactive Fe are assumed to be present (as explosion models produce only amounts insignificant for photospheric spectra).

When evaluating model properties, we group our only single-Na object, SN 2002cr, with the redshifted-Na objects: both redshifted-Na and single-Na objects lack Na components from CSM (and show ISM lines at the same time), which means they should come from similar progenitor systems.

4.1 Envelope opacity – evolution of v_{ph} with time

First, we search for evidence for a different opacity of the envelope, which may correspond to differences in the composition (or also the density structure), by looking at the time evolution of photospheric velocity v_{ph} in our models (Figure 5). For larger opacity, normally corresponding to a larger content of burned material [in particular of Fe-group elements, cf. Sauer et al. (2006)], the photosphere (in the sense of the layer where – on average over all wavelengths – an optical depth of one is reached) is expected to be further out in the envelope. Hints of a larger v_{ph} among blueshifted-Na SNe may have indeed been found by measuring Si II $\lambda6355$ Doppler velocities (blueshifts) as a proxy for v_{ph} (Foley et al. 2012b, but see Maguire et al. 2013).

The photospheric velocities in our models are highest among the blueshifted-Na SNe, and lowest among the no-Na SNe (with a noteworthy mean difference of $1000 - 2000\,\mathrm{km\,s^{-1}}$), indicating that blueshifted-Na SNe contain more opaque material in the outer layers. The redshifted-Na subsample comes to lie in between blueshifted-Na and no-Na objects, and thus shows no significant difference to the blueshifted-Na subsample or the no-Na subsample: we consider the photospheric velocities we find for each SN in this work to carry an error of $\pm1000\,\mathrm{km\,s^{-1}}$, induced by uncertainties in the data (such as uncertain distances and reddening values) and the modelling approach[8].

Benetti et al. (2005) furthermore found that SNe Ia can observationally be grouped according to the *time evolution* of their Si II $\lambda6355$ Doppler velocities (which approximate the photospheric velocity). Tanaka et al. (2008) modelled high-velocity-gradient [HVG, meaning a fast time evolution – Benetti et al. (2005)] and low-velocity-gradient (LVG) SNe and found that HVG objects have larger absolute photospheric velocities in addition to their large velocity gradient, corresponding probably to higher Fe-group mass fractions in the outer layers. The curves in Figure 5 show absolute velocity differences, but no apparent systematic difference in the gradients between the Na subsamples. In order to understand this in detail, however, one would need all our objects to have a better-sampled spectral time series (and thus model series) from early on to well past maximum [cf. e.g. the data of Benetti et al. (2005)].

4.2 Mass of Fe-group material in the outer ejecta

As a second model property to investigate, we consider the integrated Fe-group abundance. Our modelling approach allows us to determine the Fe-group content in the outer layers (above 8000 km s^{-1}) from the strength of Fe lines (which have contributions from

---

[8] We estimate the uncertainty in the fitting process to be some hundreds of km s^{-1} ($\pm$). However, the majority of the SNe modelled here have not been studied in much detail. Thus, some data suffer from less well known distance and reddening, or from wavelength-dependent errors in flux calibration. This translates into an additional uncertainty to our final model parameters.
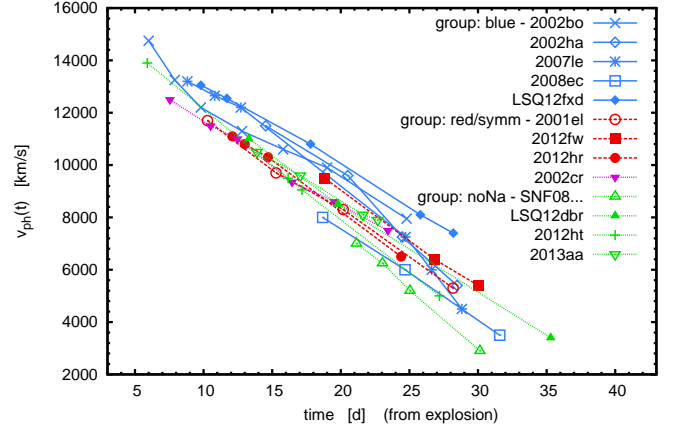
Figure 5. Evolution of photospheric velocities of our spectral models with the time passed since explosion onset. The curve style (solid/blue; dashed/red; dots/green) corresponds to the narrow Na line behaviour; different point types are used for every object.
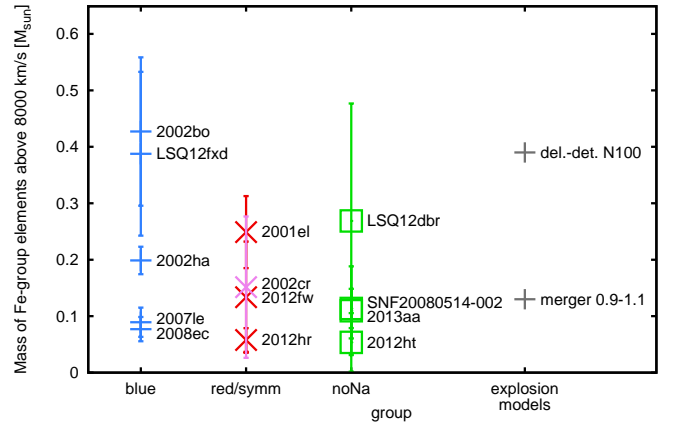
Figure 6. Mass of Fe-group elements above 8000 km s^{-1} in our spectral models, which are grouped according to the narrow Na line behaviour of the corresponding SN (left three columns). The error bars (see also text) correspond to the error introduced by (mainly statistical) uncertainties in the photospheric velocity (and thus the abundance zone borders) which we estimate to be ±1000 km s^{-1}. For comparison, we plot the corresponding masses within the hydrodynamical explosion models of Röpke et al. (2012) (right column).

directly-synthesised Fe and from decayed ^{56}Ni) and from the near-UV flux level of the SN (where all Fe-group elements, including the minor species, block the flux). We emphasise that there is some degeneracy between the effects of Fe, ^{56}Ni, and Ti/V/Cr on the spectra as long as neither UV spectra nor very early spectra (where ^{56}Ni/^{56}Co have not decayed yet) and light curves are analysed (cf. Hachinger et al. 2013). As laid out in Section 2.4, we have avoided ambiguities in this respect by using Fe-group abundance mixtures typical for certain burning zones of a SN Ia.

We plot (Figure 6, left three columns) the mass of Fe-group elements ($Z > 20$) in our spectral models integrated from 8000 km s^{-1} (down to which all our models have abundance information) outwards. The photospheric velocities in our models, giving the abundance zoning of the envelope (cf. Section 2.4.2) carry an uncertainty of ±1000 km s^{-1} (cf. Section 4.1). This is a dominant source of error in the derived *integrated* abundances which depend quite strongly on the zone borders. We have thus chosen to add error bars in Figure 6 which are generated by determining the abun-

dances with all abundance zone borders moved outwards/inwards (simultaneously) by 1000 km s^{-1}. For comparison, Figure 6 (right column) shows the Fe-group abundances within the ab-initio explosion/nucleosynthesis models of Röpke et al. (2012) on the right-hand side.

The Fe-group masses in the outer ejecta of blueshifted-Na SNe are a bit higher on average than those of other SNe. The mean values (with equal weight for each object) for the three Na subsamples and their error estimates (obtained by quadratic propagation) are:

$$M(\text{Fe-group})_{\text{blue}} = 0.24 \pm 0.04 M_\odot,$$

$$M(\text{Fe-group})_{\text{red/symm}} = 0.15 \pm 0.04 M_\odot \quad \text{and}$$

$$M(\text{Fe-group})_{\text{no-Na}} = 0.15 \pm 0.06 M_\odot.$$

As one recognises easily, the variation between the subsamples is practically within the error bars and thus hardly significant in a statistical sense. However, we remark that the differences we see between blueshifted-Na SNe and the other subsamples (both with lower Fe-group abundances), are in line with the larger opacity we suspected blueshifted-Na SNe to have after the v_{ph} analysis (Section 4.1).

Compared to the ^{56}Ni mass differences among explosion models, the variations we find are somewhat smaller. We note that the low value of Fe-group elements in the analysed layers of no-Na SNe may simply reflect a lower-than-average ^{56}Ni production in these SNe (rather than only a difference in the distribution, as expected between equally-luminous double-degenerate and single-degenerate explosions). The lower value for the no-Na subsample would then be in line with the typically lower luminosities in the explosion sites of these objects, which are mainly early-type galaxies (Hamuy et al. 2000; Gallagher et al. 2008; Maguire et al. 2013; Ashall et al. 2016a; Henne et al. 2017). For redshifted-Na SNe, a more likely explanation would be 'real' differences in the explosion properties (as luminosities are relatively similar among our redshifted-Na and blueshifted-Na objects). More objects should be investigated in the future in order to obtain statistically significant evidence.

4.3   Mass of oxygen and silicon

As a final quantitative criterion, we examine the O and Si content of the outer/intermediate layers of our models, down to 8000 km s^{-1}. In Figure 7, we have plotted the yields of our different models, and of the explosion/nucleosynthesis models of Röpke et al. (2012).

We see that no-Na and redshifted-Na objects make up their deficit in shallow Fe-group material (Section 4.2) by having a little bit more Si (cf. Mazzali et al. 2007) and somewhat more O. The explosion models show only an insignificant difference in Si mass; the difference in O mass between violent-merger and delayed-detonation models is roughly in line with the observed differences (higher mean O mass in redshifted-Na and no-Na SNe).

We see that no-Na and redshifted-Na objects make up their deficit in shallow Fe-group material (Section 4.2) by having somewhat more O (Figure 7, upper panel) and a little bit more Si (Figure 7, lower panel; see also Mazzali et al. 2007). The difference in O mass between violent-merger and delayed-detonation explosion models is roughly in line with the observed differences (higher mean O mass in redshifted-Na and no-Na SNe). In Si mass, the explosion models only show an insignificant difference to one another (with absolute values somewhat lower than the observations).
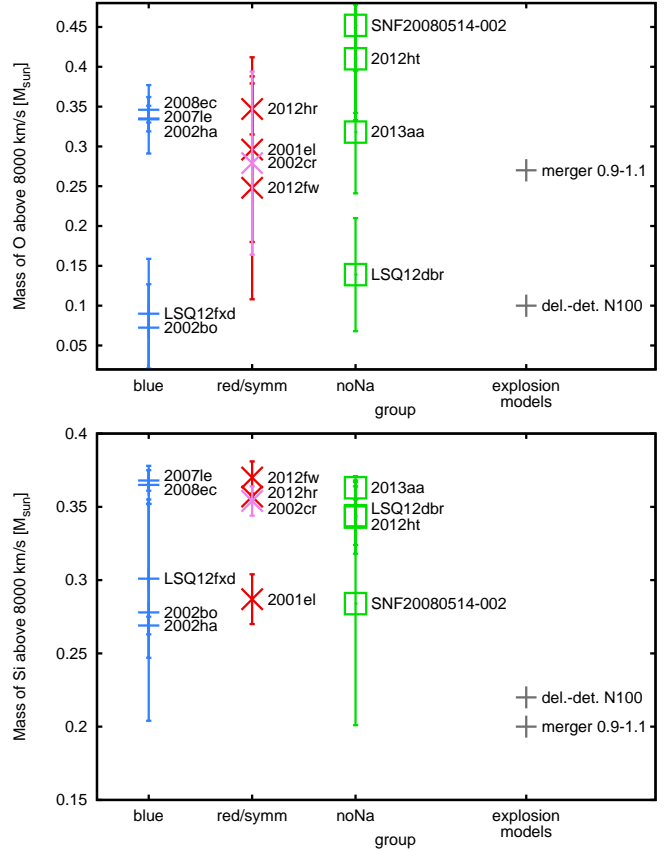
Figure 7. Mass of O (*upper panel*) and Si (*lower panel*) above 8000 km s^{-1} in our models, which are grouped according to the narrow Na I D line behaviour of the corresponding SN (left three columns, respectively). The error bars correspond to the error in v_{ph} (± 1000 km s^{-1}, as in Figure 6). For comparison, we plot the corresponding masses within the hydrodynamical explosion/nucleosynthesis models of Röpke et al. (2012) (right column within each panel). The variations in Si mass are actually relatively small (fine mass scale in lower panel) both among our SNe and the hydro models. The merger model 'compensates' for its smaller Fe-group mass in the outer layers (Figure 6) by having a larger O abundance and a significant amount of unburned C (~ 0.1 M$_\odot$, not plotted).

Owing to the relatively large scatter, the differences between the groups with respect to O[9] and Si are less clear than those we are able to see in the Fe-group statistics or in the photospheric velocities. Thus, we will mainly focus on interpreting the latter differences in the following.

4.4   Implications on SN Ia progenitors

We have found small differences between SNe displaying blueshifted-Na and other SNe; these differences exceed the typical error margins we have calculated by little or remain within them. In photospheric velocities, there is a difference of about 1000-2000 km s^{-1} between blueshifted-Na SNe and no-Na SNe (at any

---

[9]   It does not come as a big surprise that a particularly large scatter is present among our O abundances: apart from the uncertainties discussed in the sections above, the O mass of an optimised spectral model is a less-precisely determined quantity owing to weak effect of oxygen on the spectrum – O I $\lambda 7773$, the only O feature, is often contaminated by other elements' lines (mainly Mg, Si).

epoch), with redshifted-Na SNe lying in between. The lower photospheric velocities in no-Na (and redshifted-Na) SNe point towards a lower envelope opacity and probably a less efficient nucleosynthesis. Accordingly, blueshifted-Na SNe show a higher Fe-group content in the outer layers with respect to both the other subsamples.

We will now try and interpret these findings in the context of SN Ia progenitors.

4.4.1 *Theoretical expectations: differences from double- to single-degenerate explosions*

Single- and double-degenerate explosions are expected to show significant differences not only in the spatial density distribution [with possible asymmetries in double degenerates, Pakmor et al. (2010)], but also in the abundance structure (cf. Röpke et al. 2012). The (violent) white dwarf merger models of Pakmor et al. (2012) and Röpke et al. (2012), as a promising example of double-degenerate models, produce relatively large quantities of O and Si (which largely results from the burning of the secondary white dwarf) in the core of the ejecta, but also in the outer layers. Fe-group material is produced burning the dense core of the more massive white dwarf, and thus will be found in the centre of the ejecta. 3D delayed-detonation explosions, as a realistic single-degenerate model for SNe Ia (Seitenzahl et al. 2013), have less O and Si in the centre. Fe-group material is found in their core, but also further outwards (cf. Figure 4) because of the turbulent combustion in the initial deflagration phase. Quantifying the different Fe-group content in the models above $8000 \, \mathrm{km \, s^{-1}}$ (cf. Figure 6), one obtains a value of $\sim 0.4 \, \mathrm{M_\odot}$ for N100 (Seitenzahl et al. 2013) and a value of $\sim 0.1 \, \mathrm{M_\odot}$ for the $0.9 - 1.1 \mathrm{M_\odot}$ merger of Pakmor et al. (2012) and Röpke et al. (2012).

4.4.2 *Observational expectations: are different explosion types strongly linked to different Na subsamples?*

When analysing our Na subsamples for possible systematic differences caused by different progenitors, we have to ask the basic question how clearly SNe of one or another Na subsample would represent SNe from one or another explosion mechanism.

For a simplified discussion, we assume two kinds of progenitor systems to our observational subsamples – one of which is able to produce CSM ('CSM producers')[10] and the other not ('CSM-free systems'). CSM-producer objects need not always show blueshifted narrow Na lines, as the CSM may be asymmetric or very dilute. CSM-free systems, of course, can not show CSM Na lines. All systems may show random Na I D components from the ISM.

It then turns out that the probabilities of finding CSM producers in the different Na subsamples depend crucially on what fraction of SNe Ia actually come from CSM producers. In the *supplementary online material (part B)*, we have calculated these probabilities for two illustrative example scenarios (30% CSM producers or 80% CSM producers within all SNe Ia), assuming the observed Na-subsample sizes of (e.g. Maguire et al. 2013) to be representative. We have obtained the following results:

---

[10] Usually, 'CSM producers' are believed to be single degenerates, but see Phillips et al. (2013), Shen et al. (2013) and Raskin & Kasen (2013). We therefore apply a neutral naming here.

- 'Scenario 1': For a CSM-producer fraction of 30%, the majority (60%) of blueshifted-Na SNe will be CSM producers, while the no-Na and redshifted-Na subsamples will be practically devoid of these systems (contribution $\ll 10\%$). This means, the Na subsamples can be mapped relatively clearly to different progenitor types.
- 'Scenario 2': If 80% of all SNe Ia are from CSM producers, practically all blueshifted-Na SNe (90%) are CSM producers, but the no-Na and redshifted-Na subsamples are also essentially composed of these objects (70%), i.e. the difference between the Na subsamples becomes insignificant. In other words, if almost all SNe come from CSM-producer systems, all Na subsamples will have equal SN properties, and the fact that many SNe do not show CSM lines will simply be due to intrinsic effects within the explosion scenario (asymmetries etc., as mentioned).

4.4.3 *How many / which progenitor channels are at work?*

From our study, which found slight differences between the Na subsamples, we can not definitely answer the question whether 'normal' SNe Ia originate from one or two fundamental types of progenitor systems. If further studies, in the line of Sternberg et al. (2011), Foley et al. (2012b), Maguire et al. (2013) and this work, however continue to find little difference especially among redshifted-Na and blueshifted-Na SNe, we may suggest 'Scenario 2' from the previous subsection to hold: most SNe Ia are due to the same explosion mechanism(s) that is/are able to produce CSM lines. In this context, it is important to clarify whether not only single-degenerate systems (Booth et al. 2016), but also double-degenerate ones (Phillips et al. 2013; Shen et al. 2013; Raskin & Kasen 2013) can generate CSM signatures. It is also important to understand why SNe Ia in early-type galaxies tend to be fainter than average and display no narrow Na I D lines. If all SNe Ia (with redshifted/blueshifted, but also without Na lines) come from the same progenitor systems, the correlation between early-type host and lack of Na I D might be explained by what Booth et al. (2016) suggest: Na I D lines may only be visible if the CSM interacts with a relatively dense ISM.

5 CONCLUSIONS

Using radiative-transfer modelling, we have performed an abundance analysis of a sample of SNe Ia for which information on narrow Na I D absorption lines (in high-resolution spectra), as well as a decent spectral time sequence (low resolution, but good time coverage and sampling), is available. Our aim was to identify possible differences between SNe Ia with and without narrow blueshifted Na I D absorption features, and how these may relate to their explosion mechanisms. Narrow Na I D absorption lines blueshifted with respect to the SN rest frame are – at least in some cases – supposedly formed within progenitor material along the line of sight towards the observer.

The most important differences we find between our 'Na subsamples' are in photospheric velocity (where blueshifted-Na SNe show the highest values, followed by redshifted-Na SNe and no-Na SNe), and in the Fe-group content of the outer layers (where blueshifted-Na SNe show higher values than both redshifted-Na and no-Na SNe). However, all these differences are practically within error bars, such that with our sample and methods firm conclusions on SN Ia progenitors can not yet be derived.

We note that our results are compatible with those of Maguire et al. (2013), who find little difference among the subsamples showing Na I D lines (redshifted vs. blueshifted), but some larger difference between blueshifted-Na SNe and no-Na objects. Comparing the latter two subsamples, we see different photospheric velocities and Fe abundances within the outer ejecta. These correspond to a smaller overall Fe-group content in no-Na SNe, reflecting the fact that these no-Na SNe almost exclusively occur in early-type galaxies, where SNe Ia tend to have narrower light curves and a smaller luminosities (e.g. Hamuy et al. 2000). Between blueshifted- and redshifted-Na SNe, we find one significant difference in the Fe-group content of the outer layers. This may be compatible with systematic differences in the abundance stratification, possibly compatible with different explosion mechanisms. However, as long as we have only small-number statistics, this remains speculation. Mild variations, as we see them, may rather well be in line with a 'unified' SN scenario for blue- and redshifted-Na objects.

In order to clarify whether one or multiple SN Ia scenarios are at work, the differences between the Na subsamples should be further examined using much larger samples of the order of 100 objects. This becomes particularly clear looking at the expectation values of finding different explosion types within the subsamples. Unless CSM-producing systems are a minority of all SNe Ia ($\sim$ 30%), they will contribute a significant number of objects to all Na subsamples, making no-Na, redshifted-Na and blueshifted-Na SNe hardly distinguishable by any data-analysis method applied to small samples.

As more data become available, also theoretical SN Ia models should evolve, allowing for more precise checks whether observational results are compatible with them. In particular, it has to be theoretically clarified whether only single-degenerate binaries, or also double-degenerate systems can generate a CSM producing narrow Na I D components in the SN spectrum. Furthermore, a possible correlation of the CSM production in these systems with other progenitor/SN properties (such as metallicity) should be studied. Meanwhile, an analysis of peculiar SNe Ia, which we have excluded from our study and which in quite some cases have shown blueshifted Na I D lines, may help to shed further light on the progenitors of SNe Ia.

References

Ashall C., Mazzali P., Sasdelli M., Prentice S. J., 2016a, MNRAS, 460, 3529

Ashall C., Mazzali P. A., Pian E., James P. A., 2016b, MNRAS, 463, 1891

Asplund M., Grevesse N., Sauval A. J., Scott P., 2009, ARA&A, 47, 481

Baron E., Bongard S., Branch D., Hauschildt P. H., 2006, ApJ, 645, 480

Benetti S., et al., 2004, MNRAS, 348, 261

Benetti S., et al., 2005, ApJ, 623, 1011

Blondin S., Prieto J. L., Patat F., Challis P., Hicken M., Kirshner R. P., Matheson T., Modjaz M., 2009, ApJ, 693, 207

Blondin S., et al., 2012, AJ, 143, 126

Booth R. A., Mohamed S., Podsiadlowski P., 2016, MNRAS, 457, 822

Branch D., Baron E., Thomas R. C., Kasen D., Li W., Filippenko A. V., 2004, PASP, 116, 903

Branch D., Fisher A., Nugent P., 1993, AJ, 106, 2383

Brown P. J. et al., 2012, ApJ, 753, 22

Cardelli J. A., Clayton G. C., Mathis J. S., 1989, ApJ, 345, 245

Childress M. J., Filippenko A. V., Ganeshalingam M., Schmidt B. P., 2014, MNRAS, 437, 338

Chugai N. N., 2008, Astronomy Letters, 34, 389

Conley A., et al., 2006, AJ, 132, 1707

Conley A., et al., 2008, ApJ, 681, 482

Cristiani S. et al., 1992, A&A, 259, 63

Dilday B., et al., 2012, Science, 337, 942

Ferretti R., et al., 2016, A&A, 592, A40

Filippenko A. V., 1997, ARA&A, 35, 309

Firth R. E., et al., 2015, MNRAS, 446, 3895

Foley R. J., Narayan G., Challis P. J., Filippenko A. V., Kirshner R. P., Silverman J. M., Steele T. N., 2010, ApJ, 708, 1748

Foley R. J., et al., 2012a, ApJ, 744, 38

Foley R. J., et al., 2012b, ApJ, 752, 101

Gallagher J. S., Garnavich P. M., Caldwell N., Kirshner R. P., Jha S. W., Li W., Ganeshalingam M., Filippenko A. V., 2008, ApJ, 685, 752

Gamezo V. N., Khokhlov A. M., Oran E. S., 2005, ApJ, 623, 337

Ganeshalingam M., Li W., Filippenko A. V., 2011, MNRAS, 416, 2607

Ganeshalingam M., et al., 2010, ApJS, 190, 418

Gilfanov M., Bogdán Á., 2010, Nature, 463, 924

Goldhaber G. et al., 2001, ApJ, 558, 359

Goldhaber G., et al., 1998, BAAS, 193, 47.13

Greggio L., 2005, A&A, 441, 1055

Guy J. et al., 2007, A&A, 466, 11

Hachinger S., et al., 2013, MNRAS, 429, 2228

Hamuy M., Phillips M. M., Maza J., Wischnjewsky M., Uomoto A., Landolt A. U., Khatwani R., 1991, AJ, 102, 208

Hamuy M., Trager S. C., Pinto P. A., Phillips M. M., Schommer R. A., Ivanov V., Suntzeff N. B., 2000, AJ, 120, 1479

Henne V. et al., 2017, NewA, 51, 43

Hicken M., et al., 2009, ApJ, 700, 331

Hillebrandt W., Niemeyer J. C., 2000, ARA&A, 38, 191

Howell D. A., 2011, Nature Communications, 2

Iwamoto K., Brachwitz F., Nomoto K., Kishimoto N., Umeda H., Hix W. R., Thielemann F., 1999, ApJS, 125, 439

Jeffery D. J., Leibundgut B., Kirshner R. P., Benetti S., Branch D., Sonneborn G., 1992, ApJ, 397, 304

Jha S., Riess A. G., Kirshner R. P., 2007, ApJ, 659, 122

Jordan, G. C. I., Perets H. B., Fisher R. T., van Rossum D. R., 2012, ApJ, 761, L23

Kasen D., Röpke F. K., Woosley S. E., 2009, Nature, 460, 869

Kerzendorf W. E., Childress M., Scharwächter J., Do T., Schmidt B. P., 2014, ApJ, 782, 27

Kessler R., et al., 2009, ApJS, 185, 32

Kozma C., Fransson C., Hillebrandt W., Travaglio C., Sollerman J., Reinecke M., Röpke F. K., Spyromilio J., 2005, A&A, 437, 983

Krisciunas K., et al., 2003, AJ, 125, 166

Kromer M. et al., 2013, MNRAS, 429, 2287

Leibundgut B., 2000, A&A Rev., 10, 179

Lucy L. B., 1999, A&A, 345, 211

Maeda K., et al., 2016, ApJ, 816, 57

Maguire K., et al., 2013, MNRAS, 436, 222

Maoz D., Mannucci F., Nelemans G., 2014, ARA&A, 52, 107

Mattila S., Lundqvist P., Sollerman J., Kozma C., Baron E., Fransson C., Leibundgut B., Nomoto K., 2005, A&A, 443, 649

Mazzali P. A., 2000, A&A, 363, 705

Mazzali P. A., Benetti S., Stehle M., Branch D., Deng J., Maeda K., Nomoto K., Hamuy M., 2005, MNRAS, 357, 200

Mazzali P. A., Lucy L. B., 1993, A&A, 279, 447

Mazzali P. A., Podsiadlowski P., 2006, MNRAS, 369, L19

Mazzali P. A., Röpke F. K., Benetti S., Hillebrandt W., 2007, Sci, 315, 825

Mazzali P. A., et al., 2014, MNRAS, 439, 1959

Milne P. A., Brown P. J., Roming P. W. A., Bufano F., Gehrels N., 2013, ApJ, 779, 23

Nomoto K., Thielemann F., Yokoi K., 1984, ApJ, 286, 644

Ochner P., Pastorello A., Tomasella L., Benetti S., Cappellaro E., Turatto M., 2012, Central Bureau Electronic Telegrams, 3350, 1

Pakmor R., Kromer M., Röpke F. K., Sim S. A., Ruiter A. J., Hillebrandt W., 2010, Nature, 463, 61

Pakmor R., Kromer M., Taubenberger S., Sim S. A., Roepke F. K., Hillebrandt W., 2012, ApJ, 747, L10

Pastorello A., et al., 2007, MNRAS, 376, 1301

Patat F., Chugai N. N., Podsiadlowski P., Mason E., Melo C., Pasquini L., 2011, A&A, 530, A63

Patat F., et al., 2007, Science, 317, 924

Perlmutter S., et al., 1999, ApJ, 517, 565

Phillips M. M., 1993, ApJ, 413, L105

Phillips M. M., Lira P., Suntzeff N. B., Schommer R. A., Hamuy M., Maza J., 1999, AJ, 118, 1766

Phillips M. M., Wells L. A., Suntzeff N. B., Hamuy M., Leibundgut B., Kirshner R. P., Foltz C. B., 1992, AJ, 103, 1632

Phillips M. M., et al., 1987, PASP, 99, 592

Phillips M. M., et al., 2013, ApJ, 779, 38

Poznanski D., Ganeshalingam M., Silverman J. M., Filippenko A. V., 2011, MNRAS, 415, L81

Raskin C., Kasen D., 2013, ApJ, 772, 1

Riess A. G., et al., 1998, AJ, 116, 1009

Riess A. G., et al., 2007, ApJ, 659, 98

Röpke F. K., 2005, A&A, 432, 969

Röpke F. K. et al., 2012, ApJ, 750, L19

Sahu D. K., et al., 2008, ApJ, 680, 580

Sauer D. N., Hoffmann T. L., Pauldrach A. W. A., 2006, A&A, 459, 229

Scalzo R. A., et al., 2014, MNRAS, 445, 30

Schmidt B. P., et al., 1998, ApJ, 507, 46

Seitenzahl I. R. et al., 2013, MNRAS, 429, 1156

Shen K. J., Guillochon J., Foley R. J., 2013, ApJ, 770, L35

Silverman J. M., et al., 2012, MNRAS, 425, 1789

Silverman J. M., et al., 2013, ApJS, 207, 3

Sim S. A., Röpke F. K., Hillebrandt W., Kromer M., Pakmor R., Fink M., Ruiter A. J., Seitenzahl I. R., 2010, ApJ, 714, L52

Simon J. D., et al., 2009, ApJ, 702, 1157

Smartt S. J., et al., 2015, A&A, 579, A40

Soker N., 2014, MNRAS, 444, L73

Stehle M., Mazzali P. A., Benetti S., Hillebrandt W., 2005, MNRAS, 360, 1231

Sternberg A., et al., 2011, Science, 333, 856

Stritzinger M., Mazzali P. A., Sollerman J., Benetti S., 2006, A&A, 460, 793

Stritzinger M., et al., 2010, AJ, 140, 2036

Stritzinger M. D., et al., 2011, AJ, 142, 156

Strovink M., 2007, ApJ, 671, 1084

Sullivan M., et al., 2011, ApJ, 737, 102

Takanashi N., Doi M., Yasuda N., 2008, MNRAS, 389, 1577

Tanaka M., et al., 2008, ApJ, 677, 448

Thielemann F. K., Nomoto K., Yokoi K., 1986, A&A, 158, 17

Tomasella L., et al., 2014, Astronomische Nachrichten, 335, 841

Turatto M., Benetti S., Cappellaro E., 2003, in ESO Astrophysics Symposia,, Hillebrandt W., Leibundgut B., eds., Springer, Berlin, p. 200

Wang L. et al., 2003, ApJ, 591, 1110

Wang X., et al., 2008, ApJ, 675, 626

Wood-Vasey W. M., et al., 2008, ApJ, 689, 377

Yamanaka M., et al., 2009, PASJ, 61, 713

Yamanaka M., et al., 2014, ApJ, 782, L35

Yaron O., Gal-Yam A., 2012, PASP, 124, 668

APPENDIX A: THE ASSUMPTION OF THE N100 DENSITY IN OUR MODELS

As laid out in Section 2.4, we assume the density profile of the N100 model (Seitenzahl et al. 2013) for our abundance analyses. This model represents the explosion of a Chandrasekhar-mass C/O WDs as a delayed detonation. Thus, it likely corresponds to the single-degenerate path of evolution to a SN Ia. Here, we test whether this introduces systematic errors into our results for the chemical yields. We show results based on a modified version of our models, which is based on the spherically averaged density of the violent-merger explosion model of Pakmor et al. (2012) and Röpke et al. (2012). The latter model represents a SN Ia resulting from a double-degenerate system of two C/O white dwarfs with $0.9\,M_\odot$ and $1.1\,M_\odot$ (see also plot in our main text – Section 2, Figure 2).

In the upper and lower panel of Figure A1, we give the N100- and the merger-based abundance reconstruction for SN 2007le as an example case. We had to make only minor modifications to abundances/photospheric velocities to obtain an optimum fit with the merger model. The mass in both the merger and the delayed-detonation model above $v = 8000\,\mathrm{km\,s^{-1}}$ (i.e. in the envelope zone we have modelled) is $\sim 0.9\,M_\odot$, such that also the integrated chemical yields are similar.

Therefore, when repeating our analyses of Section 4 with the merger-based models for all our SNe, we obtain only insignificant differences. An example for this is shown in Figure A2. Here, the mass of Fe-group elements above $v = 8000\,\mathrm{km\,s^{-1}}$ we derive is shown for all SNe, first for our 'standard models' (upper panel, see also Section 4.2) and then for our merger-based models (lower panel). Realising that the changes are minor, we are confident that our conclusions would not be changed if we would use the merger model as a basis for all our analysis or for part of it.

We caution that both our N100- and our merger-based models are calculated with 1-D-averaged density profiles of the respective explosion models. In terms of fit quality, the results we obtain with these averaged density profiles are sometimes not as good as results obtained with a density from 1-D explosion models such as W7 or WDD1 (Nomoto et al. 1984; Iwamoto et al. 1999). The discrepancies between models and observations, which may be due to the hydrodynamical models themselves or to the 1-D averaging, correspond to an uncertainty in our abundance results which we estimate to be within the error bars shown in Section 4. In forthcoming studies with larger SN Ia samples, where the entire analysis reaches a finer (i.e. statistically more significant) level, this source of error should however be thoroughly investigated.
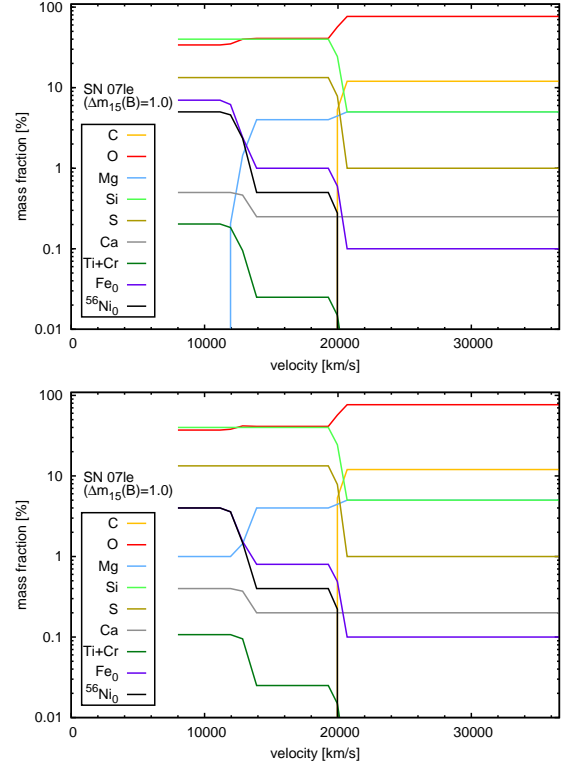
Figure A1. *Upper panel:* Abundance distribution of our (N100-based) standard model for 2007le (already shown in Figure 4). *Lower panel:* Abundance distribution of the test model based on the merger density.
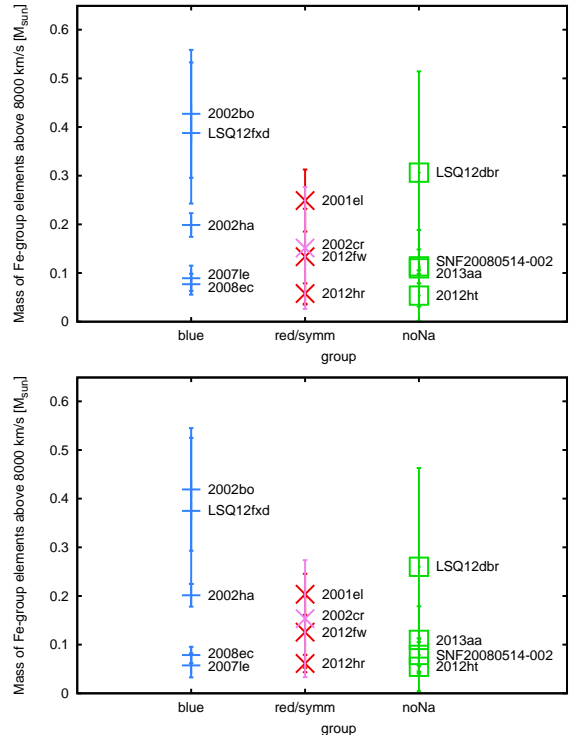
Figure A2. Mass of Fe-group elements above $8000\,\mathrm{km\,s^{-1}}$ in our models based on N100 (*upper panel*, which is a copy of Figure 6 of the main text), and in our test models based on the $0.9 - 1.1\,M_\odot$ merger density (*lower panel*). The differences in density between N100 and the merger model have no pronounced effect on the chemical yields of our models.